

Supporting information

Materials

All the reagents are purchased without further purification. The water used in experiments is self-made ultrapure water with electrical resistivity 18 M Ω ·cm. Acetonitrile (ACN, HPLC grade, water content < 30 ppm) is obtained from Fisher Chemical (USA). N, N-dimethylformamide (DMF, AR, 99.5%, water content < 0.1%) and Dimethyl sulfoxide (DMSO, AR, 99%, water content < 0.2 %), anhydrous acetonitrile (water content < 10 ppm), CdCl₂·2.5H₂O, Zn(Ac)₃·6H₂O, NaOH, 5,5-dimethyl-1-pyrroline N-oxide (DMPO), oxalic acid (AO), Benzoquinone (BQ), sodium azide (NaN₃), Butylated hydroxytoluene (BHT), HMF (98%), DFF, FFCA, H₂O₂, H₂¹⁸O, D₂O, benzyl alcohol and its derivatives, 2-Pyridinemethanol, 2-Thiophenemethanol and Cyclohexanol et al. are all purchased from Aladdin Bio-Chem Technology Co., LTD, Shanghai.

Physical characterization

X-ray diffractometer (XRD, Rigaku Smartlab) with Cu K α radiation ($\lambda = 0.154$ nm) was used to determine the crystal structure of samples. Energy dispersive spectrum (EDS) and transmission electron microscopy (Tecnai G2 F30) were collected to analyze the morphology of photocatalyst. The UV/vis spectrophotometer (Shimadzu UV-3600) was employed to analyze the photoresponse properties of the catalysts. In order to further study the chemical composition of samples, X-ray photoelectron spectroscopy (XPS, Kratos AXIS NOVA spectrometer) was performed. The Brunauer-Emmett-Teller (BET) method was used to determine the specific surface area.

Sample preparation

In detail, 1.713 g CdCl₂·2.5H₂O and 0.549 g Zn(Ac)₂·2H₂O were dispersed in 50 mL DI water and stirred for 5 min. After that, 10 ml of 2 M NaOH solution and 1.141 g of thiourea were added into the suspension. Then, the suspension was further stirred for 30 min and transferred into 100 mL of stainless-steel autoclave, maintained at 180 °C for 18 h. Finally, the obtained precipitates were collected and washed. The final products were dried at 60 °C for 6 h. The Cd_xZn_{1-x}S nanoparticles with different elementary ratio were fabricated by using different amount CdCl₂·2.5H₂O and Zn(Ac)₂·2H₂O.

For loading different metal co-catalyst: 100 mg Cd_{0.5}Zn_{0.5}S nanoparticles was dispersed into 40 mL water containing 50 μ L of 2 M NaOH. After ultrasonic for 30 min, certain amount of Co(NO₃)₂·6H₂O, Ni(NO₃)₂·6H₂O, Cu(NO₃)₂, PdCl₂, AgNO₃, HAuCl₄, H₂PtCl₆ solution was added into the suspension and stirred for 15 min. Subsequently, 10 mL fresh NaBH₄ (2 M) solution was added into the suspension dropwise, after further stirring for 30 min, the obtained green suspension was centrifuged and dried in vacuum.

Other catalysts preparation

For CdS: 1.713 g CdCl₂·2.5H₂O was dispersed in 50 mL DI water and stirred for 5 min. After that, 5 ml of 2 M NaOH solution and 0.571 g of thiourea were added into the suspension. Then, the suspension was further stirred for 30 min and transferred into 100 mL of stainless steel autoclave, maintained at 180 °C for 18 h. Finally, the obtained precipitates were collected and washed. The final products were dried at 60 °C for 6 h.

For Mn_{0.2}Cd_{0.8}S: 1.713 g CdCl₂·2.5H₂O and 1.225 g Mn(CH₃COO)₂·4H₂O were dispersed in 40 mL DI water and stirred for 5 min. After that, 20 ml of 2 M NaOH solution and 1.141 g of thiourea were added into the suspension. Then, the suspension was further stirred for 30

min and transferred into 100 mL of stainless-steel autoclave, maintained at 180 °C for 18 h. Finally, the obtained precipitates were collected and washed. The final products were dried at 60 °C for 6 h.

For ZnIn₂S₄: InCl₃ (1 mmol), Zn(CH₃COO)₂·2H₂O (0.5 mmol), and thioacetamide (6 mmol) were orderly dissolved into 50 mL deionized water, and then stirred at room temperature for 30 min. Thereafter, the clear solution was poured into 100 mL stainless steel. autoclave, and maintained at 180 °C oven for 18 h.

For CdIn₂S₄: the steps are same as those of ZnIn₂S₄, excepting using Cd(CH₃COO)₂·2H₂O instead of Zn(CH₃COO)₂·2H₂O.

For carbon doped g-C₃N₄, firstly, 1.5 g of 2,4,6-triaminopyrimidine and 1g of melamine are thoroughly mixed under grinding, then transferred to a porcelain boat. Subsequently, the porcelain boat is placed in a tube furnace and kept at 600 °C in a nitrogen atmosphere for two hours, with a heating rate of 2 °C/min. After natural cooling, the sample is removed and thoroughly ground for future use.

Photocatalytic HMF oxidation

The photocatalytic HMF oxidation was carried out via a photochemical reactor equipped with 445 ± 10 nm LED (20 W). Typically, 20 mg catalyst was dispersed in 15 mL quartz tube containing 10 mL reaction solution with HMF concentration of 10 mM (unless otherwise noted). A mixed solution of water and ACN (HPLC grade ACN with H₂O content at 30 ppm) is employed unless stated.) are used as reaction solution (V_{ACN}+V_{H₂O}=10 mL), in which the water addition volume are controlled to be 0.02 mL, 0.04 mL, 0.08 mL, 0.16 mL, 0.20 mL, 0.30 mL, 0.50 mL, 0.75 mL, 1.70 mL, 2.30 mL, 3.3 mL, 5.0 mL, 7.0 mL, 9.0 mL, 10.0 mL. After ultrasonic treatment for 4 min, the suspension is employed under air atmosphere for reaction, and sampling after certain reaction time. The other solvents (DMF, DMSO, water) are also employed for comparison under air atmosphere. For different atmosphere, the air in the reactor was extracted first by vacuum pump, and then N₂ or O₂ is injected.

For other alcohol substrates and catalysts: the procedures are same as above HMF oxidation excepting add different feedstocks in the reaction solution of 10 mL ACN or ACN + H₂O.

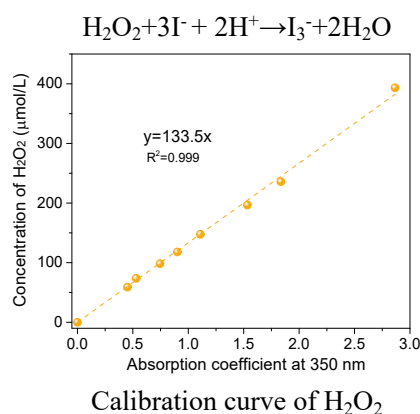
The products yield=(the amount of specific product/initial amount of HMF)×100%, HMF conversion=(the initial amount of HMF - the residual amount of HMF)/the initial amount of HMF×100%, The mineralization percentage=(the initial amount of HMF - the overall amount of detected products)/the initial amount of HMF×100%.

Products quantification

High-performance liquid chromatography (HPLC) on a WATERS 2695 with an ultraviolet-visible detector was employed for quantification of HMF, DFF, FFCA and FDCA (Wavelength: 248 nm. Column: Bio-Rad, Aminex HXP-87P. Mobile phase: 5 mM H₂SO₄. Flow rate: 0.6 mL/min). For other alcohol substrates, Agilent 7890A equipped with FID detector and gas chromatograph-mass spectrometer (GC-MS, GC 7890A/5975C inert XL MSD) were used for quantification. The possible gas product through photocatalytic process was quantified by gas chromatography (Agilent 7890 equipped with a Molecular Sieve packed column, and a thermal conductivity detector). The identification and quantification of the products were determined via the calibration curves by applying standard solutions with known concentrations of commercially

purchased pure reactants, intermediates, and products.

The produced H_2O_2 was quantified by reagent color-developing method. First, 1 mL filtered reaction solution was attenuated by 2 mL DI water, after that, 1 mL of the attenuated sample was added into a mixed solution of 1 mL KI (0.4 M) aqueous solution and 1 mL commercial pH buffer with pH=4 (potassium biphthalate). Finally, the solution was kept for 1 h in dark. The H_2O_2 concentration can be determined by the triiodide anions (I_3^-) concentration according to the following equation, where the I_3^- can be estimated by Lambert-Beer's law due to their strong absorbance at 350 nm.



Quenching Experiment

The quenching experiments of active species were conducted by adding extra radical scavengers (general condition: 10 mg/30 μL scavengers in 10 mL reaction solution) to investigate the role of radicals during photocatalytic HMF selective oxidation to DFF. 5,5-dimethyl-1-pyrroline-N-oxide (DMPO) was employed as radicals scavenger. Benzoquinone (BQ), NaN_3 , oxalic acid ($\text{H}_2\text{C}_2\text{O}_4$), and Butylated hydroxytoluene (BHT) were added as scavengers for superoxide radicals, singlet oxygen, H_2O_2 , and carbon central radical, respectively.

Photochemical characterization

To prepare the working electrodes, 5.0 mg catalyst was dispersed in 15 mL deionized water and then sonicated for 20 min. Subsequently, 1 mL of the solution was dropped homogeneously on a 2 cm \times 3 cm fluoride-doped tin oxide (FTO) glass. After drying at ambient temperature, the FTO working electrodes were used without further processing.

Transient photocurrent (i-t) and Mott-schottky (M-S) curves were performed with the electrochemical workstation (CHI660E, Chenhua in Shanghai) in 0.1 M Na_2SO_4 electrolytes by employing Ag/AgCl electrode as the reference electrode and Pt foil as the counter electrode. The bias of 0.5 V was used for the photocurrent test.

Catalyst regeneration

Upon completion of the reaction, the acetonitrile suspension containing the catalyst powder was poured into a 0.1M Na_2S aqueous solution and stirred for 4 hours. Subsequently, the resulting suspension was subjected to centrifugation, followed by two separate centrifugations with water and ethanol, respectively. The solid obtained from this process was then dried and collected for future use.

In situ ATR-SEIRAS spectroscopy measurement

The surface enhanced infrared absorption spectroscopy with the attenuated total reflection configuration was employed. A Thermo Nicolet 8700 spectrometer equipped with MCT detector cooled by liquid nitrogen was employed for the electrochemical ATR-SEIRAS measurements. Chemical deposition of Au thin film (~60 nm) on the Si prism was prepared according to “two-step wet process”. Before chemical deposition of Au, the Si prism surface for IR reflection was polished with Diamond suspension and cleaned in water with sonication. Then the prism was soaked in a piranha solution (7:3 volumetric ratio of 98% H₂SO₄ and 30% H₂O₂) for 2 hours. 30 uL 10 mM HMF solution containing catalyst was deposited on the Au-film, the light intensity was controlled to be ~50 mW/cm². All spectra were shown in $\Delta R/R=(E_s-E_R)/E_R$, with E_s and E_R representing the sample and reference spectra, respectively. The spectral resolution was 4 cm⁻¹ for all the measurements if not otherwise mentioned.

DFT method

The electron exchange and correlation were described with GGA-PBE functiona (1-3). The localized double-numerical quality basis set with a polarization d-function (DNP-4.4 file) was chosen to expand the wave functions (2,4). For the weak interaction, the DFT-D2 (Grimme) method was used (5). The core electrons of the metal atoms were treated using the effective core potentials (ECP) (2,6), and the orbital cutoff was 4.0 Å for all atoms. For the geometry optimization, the convergences of the energy, maximum force, and maximum displacement were set as 2×10^{-5} Ha, 4×10^{-3} Ha/Å, and 5×10^{-3} Å, and the SCF convergence for each electronic energy was set as 1.0×10^{-5} Ha. The vibrational frequency analysis was performed to gain the thermodynamic results (7). The TS of all the elementary reaction steps was searched using the linear synchronous transit and the quadratic synchronous transit (LST/QST) method on the same calculation standard (8). For the reactions with the solvent, the calculations were performed using the COSOM method, which the solvent is water and its dielectric constant is 78.54.

Molecular dynamic Method

For pure ACN: Cubic cells of size 7.66 nm were used for bare C₂H₃N: (including one Cd₃ZnS₄, three C₆H₆O₃ and 9200 C₂H₃N). For ACN+160 uL H₂O: Cubic cells of size 9.19 nm were used for 1.6% H₂O: (including one Cd₃ZnS₄, three C₆H₆O₃, 239 H₂O and 9010 C₂H₃N). For ACN+1.7 mL H₂O: Cubic cells of size 9.06 nm were used for 17% H₂O: (including one Cd₃ZnS₄, three C₆H₆O₃, 2506 H₂O and 7598 C₂H₃N). For pure H₂O: Cubic cells of size 7.54 nm were used for bare H₂O: (including one Cd₃ZnS₄, three C₆H₆O₃ and 14000 H₂O). A modified velocity-rescaling thermostat was used to maintain the temperature at 298 K, and setting the coupling time constant to 0.1 ps. A semi-isotropic Parrinello-Brahmanbaria was used to maintain the pressure at 1 bar. The Particle Mesh Ewald method was used to deal with electrostatic interactions. The total simulation time is 10 ns to obtain the equal product.

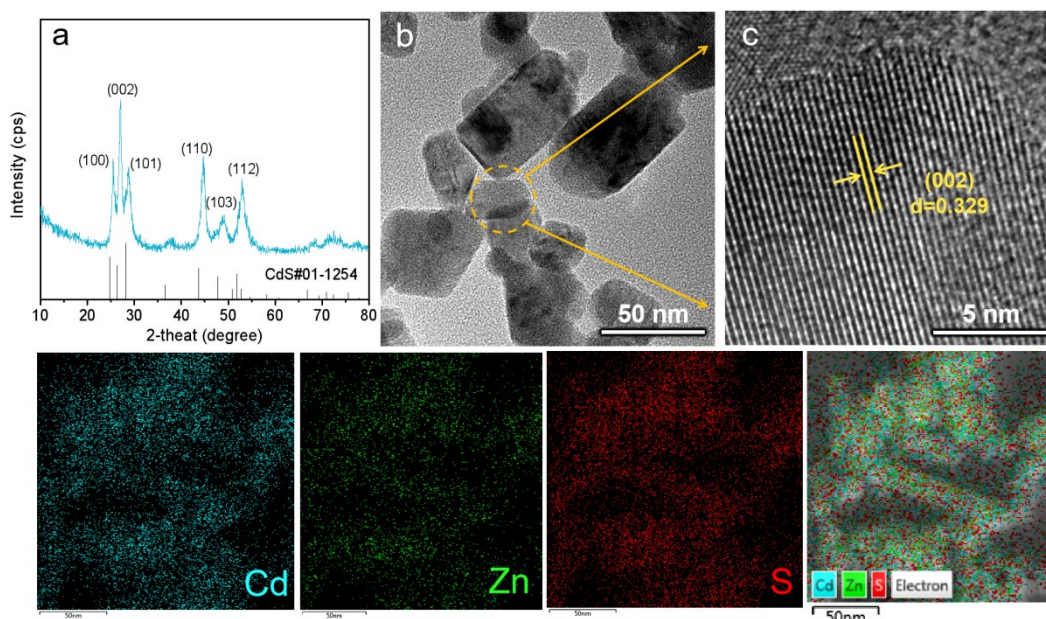


Fig.S1 XRD x-ray diffraction curve, (b-c) TEM images, and Mapping images of $\text{Cd}_{0.75}\text{Zn}_{0.25}\text{S}$ nanoparticles.

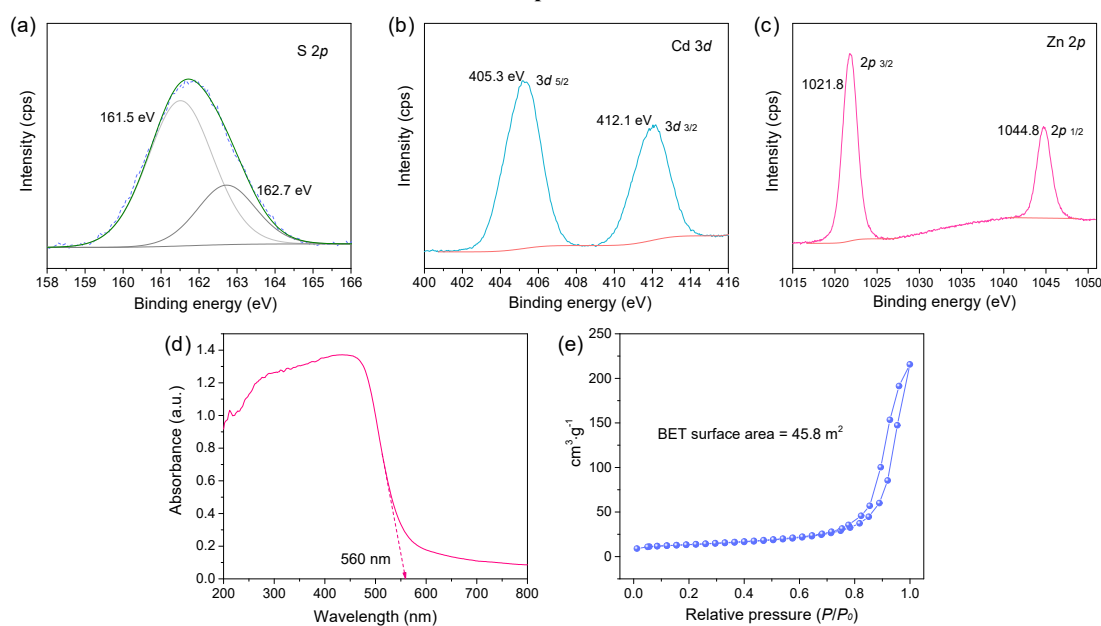


Fig.S2 (a-c) High-resolution XPS of Zn Cd and S of $\text{Cd}_{0.75}\text{Zn}_{0.25}\text{S}$; (d) Band gaps of $\text{Cd}_{0.75}\text{Zn}_{0.25}\text{S}$ according to Kubelka-Munk plots; (e) N_2 adsorption-desorption isotherms of $\text{Cd}_{0.75}\text{Zn}_{0.25}\text{S}$

$\text{Cd}_{0.75}\text{Zn}_{0.25}\text{S}$ nanoparticle was prepared using a typical hydrothermal method. The XRD (Fig.S1a) peaks of $\text{Cd}_{0.75}\text{Zn}_{0.25}\text{S}$ shift to higher angle comparing with the JCPD card of hexagonal CdS, which is resulted from reduced crystal lattice spacing as a consequence of the incorporation of Zn into the crystal cell of CdS. TEM (Fig.S1(b-c)), mapping images (Fig.S1(d-f)) and XPS (Fig.S2(a-c)) give further evidences on the successful preparation of $\text{Cd}_{0.75}\text{Zn}_{0.25}\text{S}$ nanoparticles. These nanoparticles exhibit a good response to the 450 nm light source according to UV-vis absorption spectrum (Fig.S2d). The band gap of $\text{Cd}_{0.75}\text{Zn}_{0.25}\text{S}$ nanoparticles is determined to be 2.33 eV by Kubelka-Munk plots in Fig.S3a, and its conduction band (CB) potential locates at -0.45 eV (vs. SHE), according to Mott-Schottky analysis (Fig.S3b). The valence band maximum is therefore located at 1.88 eV (vs. SHE), suggesting that $\text{Cd}_{0.75}\text{Zn}_{0.25}\text{S}$ nanoparticles cannot oxidize

H₂O into ·OH ($E(\cdot\text{OH}/\text{H}_2\text{O}) = +2.7 \text{ eV}$), but can produce ·O₂⁻ via electron transfer from CB to O₂ ($E(\text{O}_2/\cdot\text{O}_2^-) = -0.33 \text{ eV}$).

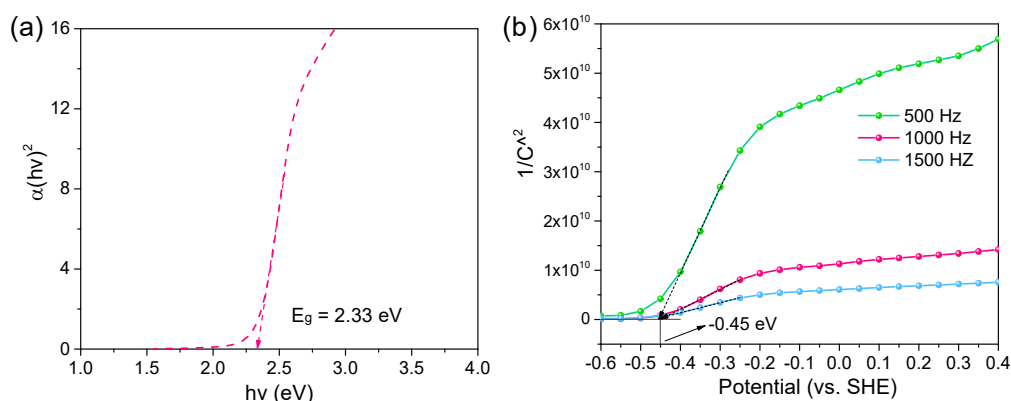


Fig.S3 (a-b) Kubelka-Munk plots and Mott-schottky curves of Cd_{0.75}Zn_{0.25}S under different frequency at pH=7.

The band gap of Cd_{0.75}Zn_{0.25}S nanoparticles is determined to be 2.33 eV, and the conduction potential (after correction) is determined to be -0.45 eV after calculation, and the valence potential is 1.88 eV. That means Cd_{0.75}Zn_{0.25}S nanoparticles cannot oxidize H₂O into ·OH, but can produce ·O₂⁻ via electron transfer from CB to O₂.

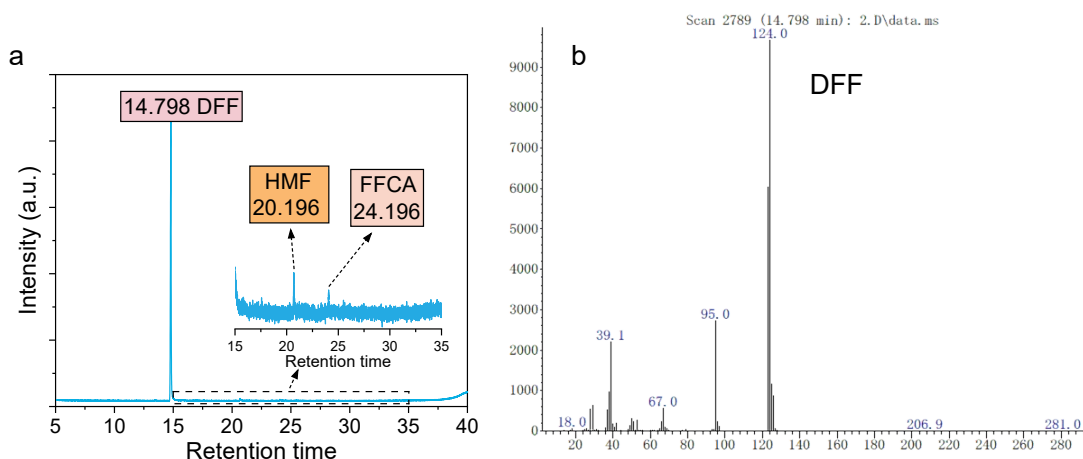


Fig.S4 (a) GC-MS spectrum of the sample after reaction in the presence water in ACN, (b) the MS/MS spectrum of produced DFF.

The GC-MS was collected after reaction, the indicated almost no other carbon-containing organic products can be detected in the solution except DFF, HMF and FFCA. This result suggests that the portion deviating from the carbon balance almost entirely converted to inorganic carbon, such as CO₂ and other species, which is also supported by the CO₂ peak in the in-situ ATR-SEIRS spectra (Fig.6 in main text).

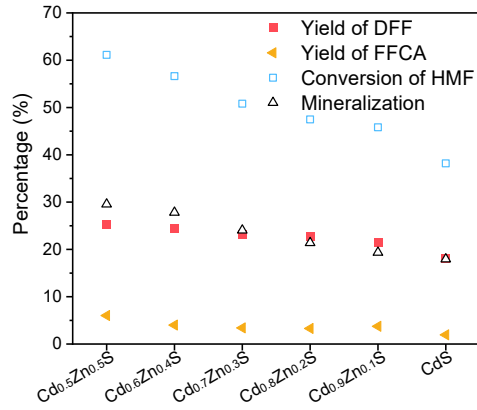


Fig. S5 HMF selective oxidation activity of Cd_xZn_{1-x}S (x= 0.5, 0.6, 0.7, 0.8, 0.9, 1.0);

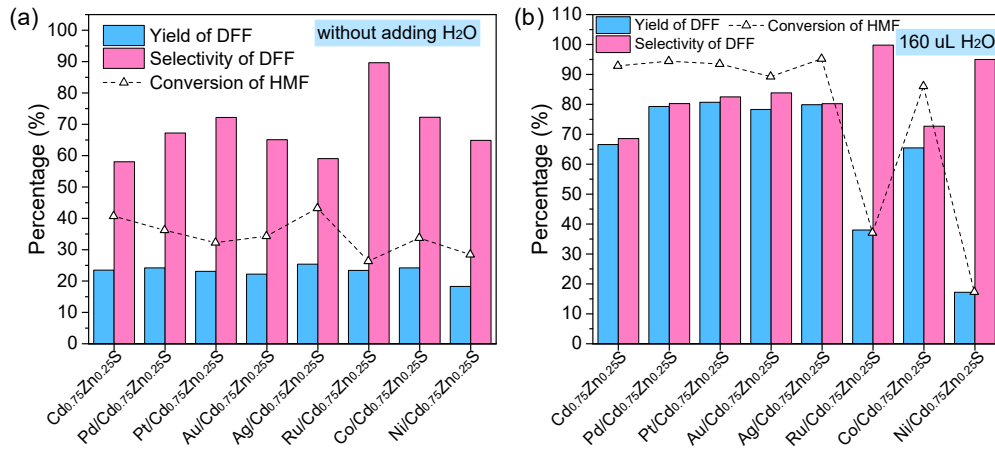


Fig.S6 Control experiment in ACN or ACN + 160 uL H₂O with loading different co-catalyst over bare Cd_{0.75}Zn_{0.25}S.

Tab.S1 The comparison of DFF yield and HMF with or without adding H₂O over kinds of metal modified Cd_{0.75}Zn_{0.25}S

Catalysts	Without adding H ₂ O		Adding 160 uL H ₂ O	
	Yield (%)	Selectivity (%)	Yield (%)	Selectivity (%)
CZS	23.5	58.1	66.6	68.6
0.5%-Pd/CZS	24.2	67.2	79.3	80.3
0.5%-Pt/CZS	23.1	72.2	80.7	82.5
0.5%-Au/CZS	22.2	65.1	78.3	83.8
0.5%-Ag/CZS	25.4	59.1	79.9	80.2
0.5%-Ru/CZS	23.4	89.7	38.0	99.8
1%-Co-CZS	24.2	72.6	65.5	72.7
1%-Ni/CZS	18.1	64.9	17.1	94.5

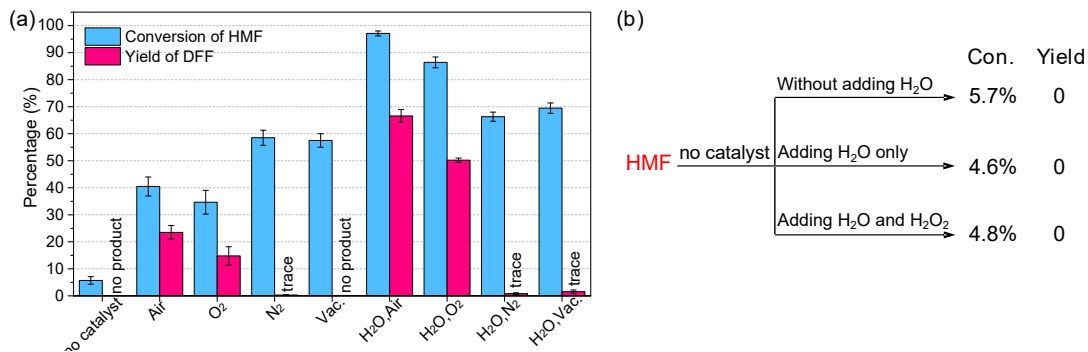


Fig.S7 Control experiment in ACN or ACN+ 160 μ L H₂O under different conditions over bare Cd_{0.75}Zn_{0.25}S (water content: 160 μ L).

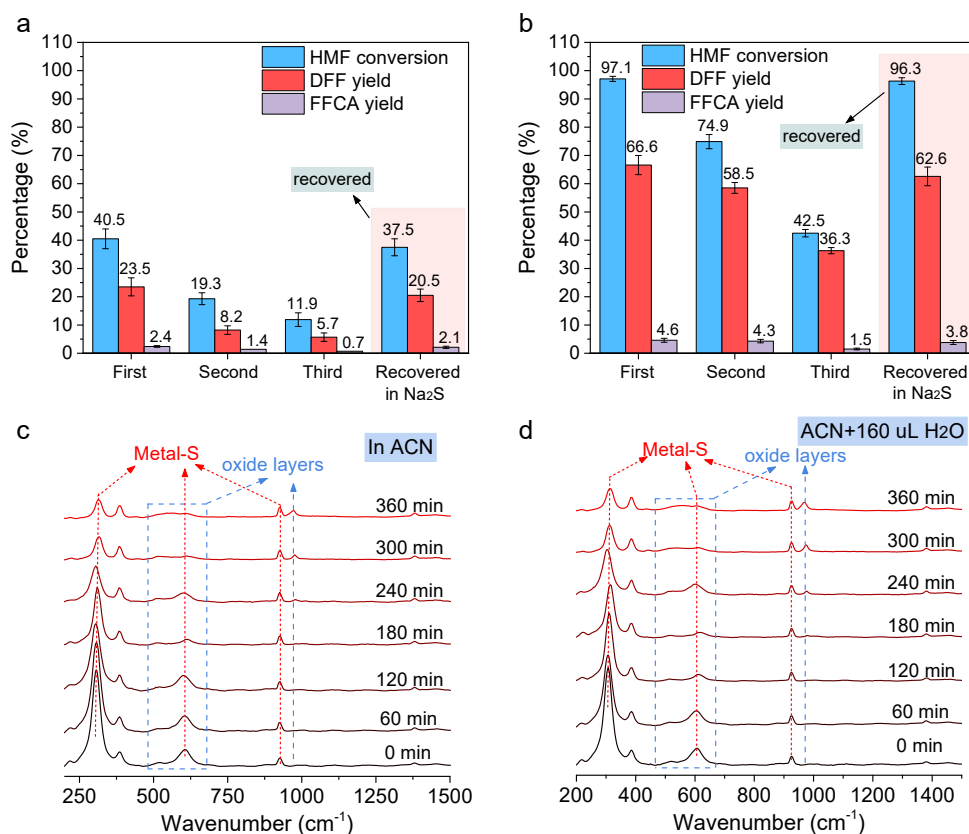
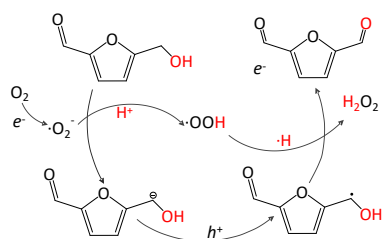


Fig. S8 (a-b) Cycling experiment of bare Cd_{0.75}Zn_{0.25}S in the absence and presence of water in ACN. (c-d) In-situ surface enhanced Raman spectrum of bare Cd_{0.75}Zn_{0.25}S in ACN with and without adding 160 μ L H₂O.

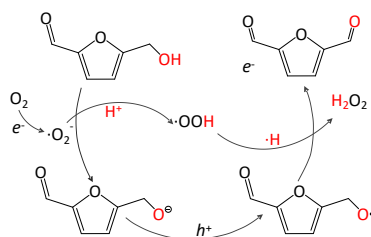
As shown in Fig.S8, the peaks at 314 cm⁻¹, 606 cm⁻¹ and 929 cm⁻¹ can be attributed to the Metal-S bond in Cd_{0.75}Zn_{0.25}S, the decreased peak intensity suggest surface S losing caused by the well-known photocorrosion along with extended reaction time, whatever water was added or not.³⁰⁻³¹ The broad band located around 480 cm⁻¹ to 680 cm⁻¹ and peak appearing at 971 cm⁻¹ are ascribed to the newly emerged oxide layers due to surface S losing.³²

Reaction path 1:



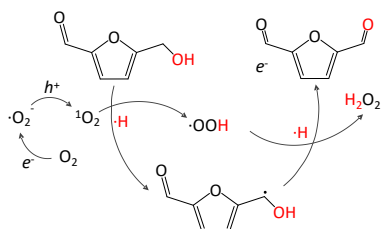
- (1) $e^- + O_2 \rightarrow \cdot O_2^-$
- (2) $R-CH_2OH + \cdot O_2^- \rightarrow R-CHOH + \cdot OOH$
- (3) $R-CHOH + h^+ \rightarrow R-CHO$
- (4) $R-CHOH + \cdot OOH \rightarrow DFF + H_2O_2$

Reaction path 2:



- (1) $e^- + O_2 \rightarrow \cdot O_2^-$
- (2) $R-CH_2OH + \cdot O_2^- \rightarrow R-CH_2O^- + \cdot OOH$
- (3) $R-CHOH + h^+ \rightarrow R-CH_2O^-$
- (4) $R-CHOH + \cdot OOH \rightarrow DFF + H_2O_2$

Reaction path 3:



- (1) $e^- + O_2 \rightarrow \cdot O_2^-$
- (2) $h^+ + \cdot O_2^- \rightarrow {}^1O_2$
- (3) $R-CH_2OH + {}^1O_2 \rightarrow R-CHOH + \cdot OOH$
- (4) $R-CHOH + \cdot OOH \rightarrow DFF + H_2O_2$

Fig S9 Previous proposed reaction pathways of HMF to DFF in literatures.

Tab. S2 The relationship between HMF conversion, DFF yield and selectivity, and mineralization percent with H₂O content

H ₂ O Content (mL)	HMF Con. (%)	DFF yield (%)	FFCA yield (%)	Mineralization (%)	DFF Sel. (%)
0	40.5±3.5	23.5±3.2	2.3±0.3	14.5±1.7	58.2±3.9
0.02	45.1±2.6	26.1±2.2	2.6±0.3	16.4±3.6	57.9±4.3
0.04	50.6±3.3	29.5±1.4	3.2±0.8	19.1±1.4	58.2±2.2
0.08	93.1±1.1	63.7±3.1	4.0±0.1	24.1±3.0	68.4±3.3
0.16	97.2±0.9	66.6±2.4	4.6±0.7	25.7±1.4	68.5±2.5
0.20	98.5±1.2	64.8±1.7	5.3±0.5	28.1±2.6	65.8±1.7
0.30	95.4±2.7	61.3±1.5	4.2±0.6	29.7±2.0	64.3±1.6
0.50	90.5±3.2	53.8±2.1	4.1±0.6	32.4±2.7	59.4±2.3
0.75	67.0±4.2	36.6±3.1	2.4±0.3	27.8±3.1	54.6±4.7
1.0	36.4±1.9	15.5±2.0	1.3±0.1	19.4±2.5	42.6±5.5
1.70	14.0±1.5	4.4±0.5	0.4±0.1	9.1±1.8	31.4±3.6
2.30	17.5±1.7	4.9±0.4	0.5±0.1	11.8±1.9	28.0±2.3
3.30	40.6±2.1	9.0±1.0	1.1±0.2	30.1±2.0	22.2±2.5
5.0	92.0±1.9	15.9±2.1	7.6±0.4	67.3±2.6	17.3±2.3
7.0	97.0±3.4	10.6±2.5	8.8±0.5	77.6±2.7	10.9±2.6
9.0	99.7±0.4	7.6±0.8	8.6±0.4	82.6±3.5	7.6±0.8
10.0	99.4±0.6	4.4±0.7	4.8±0.3	90.0±3.2	4.4±0.7

Tab.S3 The conversion, yield and mineralization percent under different condition in ACN or ACN+ 160 uL H₂O.

Conditions	Conversion (%)	Yield of DFF (%)	Mineralization (%)
Air	40.6±3.5	23.5±2.5	14.5±1.7
H ₂ O, Air	97.1±0.9	66.6±2.4	25.6±2.6
O ₂	34.7±4.4	14.8±3.4	17.7±3.6
H ₂ O, O ₂	86.4±2.0	50.2±0.8	34.0±3.8
N ₂	58.5±2.8	0.3±0.1	53.2±2.5
H ₂ O, N ₂	66.3±1.7	0.8±0.3	65.5±1.7
Vac.	57.5±2.5	N/A	57.5±2.5
H ₂ O, Vac.	69.5±1.9	1.6±0.6	65.1±1.9
Without catalyst, Air	5.7±1.4	N/A	5.7±1.4

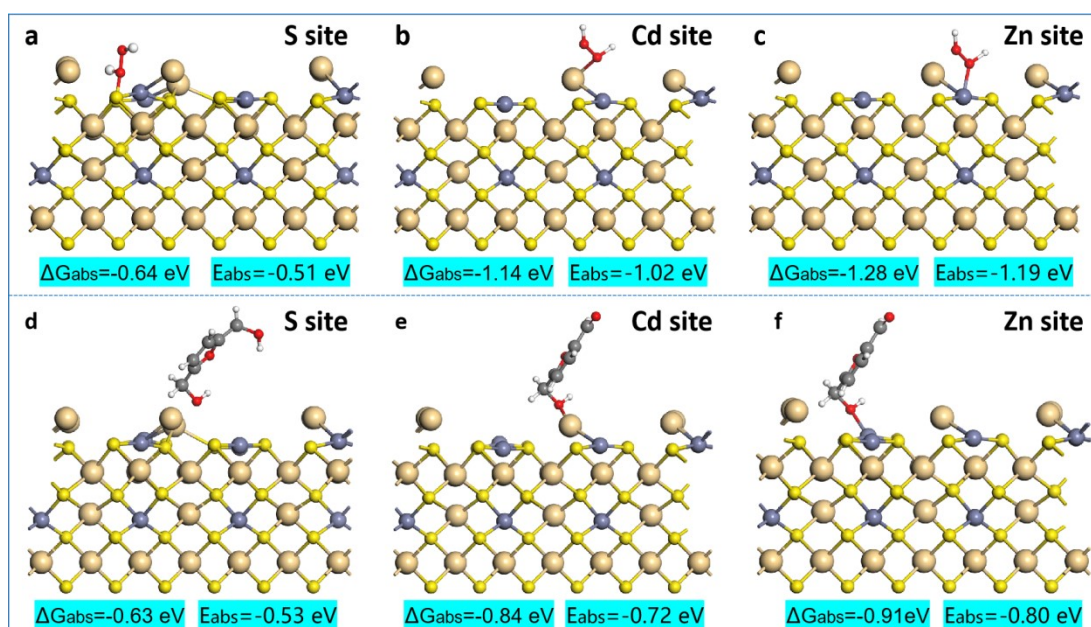


Fig.S10 (a-c) H₂O₂ adsorption structure on the surface of CZS (002) at different sites: a: S site, b: Cd site, c: Zn site. (d-f) HMF absorption structure on the different sites of Cd_{0.75}Zn_{0.25}S (002) (a: S site, b: Cd site, c: Zn site),

The result here indicates H₂O₂ and HMF both tends to absorb on Zn site. The calculated free energies of adsorption for H₂O₂ at the S, Cd, and Zn sites are -0.64 eV, -1.14 eV, and -1.28 eV, respectively. It is evident that the most stable adsorption state of H₂O₂ is formed on the Zn atom, with a corresponding adsorption energy of 1.19 eV.

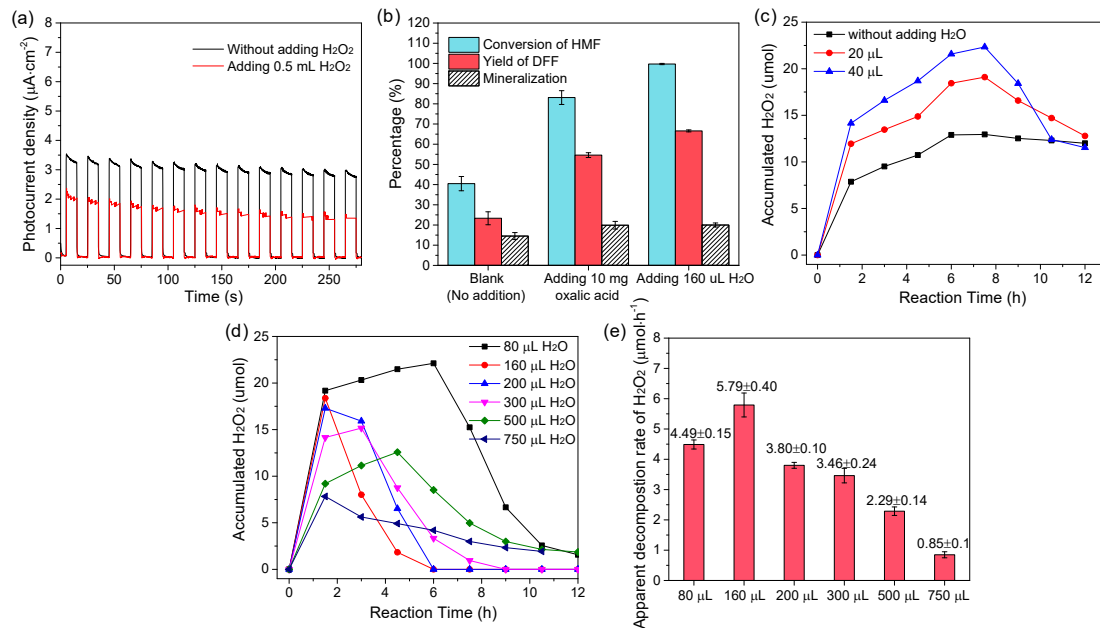


Fig.S11 HMF conversion and DFF yield comparison with different additions using $\text{Cd}_{0.75}\text{Zn}_{0.25}\text{S}$; (a) Transient photocurrent of $\text{Cd}_{0.75}\text{Zn}_{0.25}\text{S}$ in the presence and absence of 0.5 mL H_2O_2 ; (b) The comparison of activities by adding 10 mg oxalic acid and 160 μL H_2O in ACN, (c-d) Time-dependent H_2O_2 evolution with adding different amount H_2O in ACN; (e) The apparent H_2O_2 decomposition rate over different solution conditions.

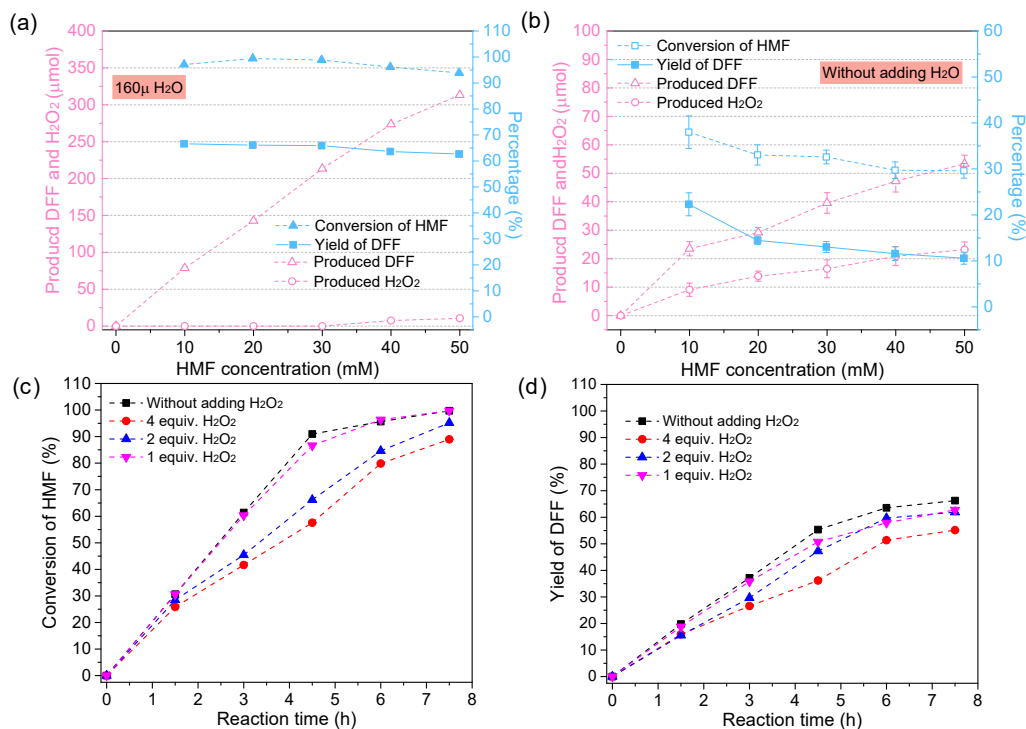


Fig.S12 (a-b) The correlation between initial HMF concentration and HMF conversion using bare $\text{Cd}_{0.75}\text{Zn}_{0.25}\text{S}$, DFF yield and H_2O_2 productivity in ACN or ACN + 160 μL H_2O using bare $\text{Cd}_{0.75}\text{Zn}_{0.25}\text{S}$; (c-d) Time-dependent HMF conversion and DFF yield after adding certain amount of H_2O_2 using bare $\text{Cd}_{0.75}\text{Zn}_{0.25}\text{S}$.

Tab.S4 Performance comparison of current studies on photocatalytic HMF to DFF

Catalysts (mg)	Solvents (mL)	HMF (mM)	Time (h)	Conv. (%)	Yield. (%)	Rate ($\mu\text{mol}\cdot\text{h}^{-1}$)	Refs.
MAPbBr ₃ (40 mg)	ACN (10 mL)	5.0	10	100	90±1.2	4.5	9
Nb ₂ O ₅ (50 mg)	BTF (5 mL)	0.1	6	19.2	17.4	0.014	10
WO ₃ /g-C ₃ N ₄ (50 mg)	ACN/BTF (3/2,5 mL)	0.1	6	27.4	23.9	0.02	11
P-Cd _{0.5} Zn _{0.5} S (1 mg)	Water (5 mL)	16	8	40	26	2.6	12
TiO ₂ (30 mg)	Water (150 mL)	0.5	16.3	50	13	0.6	13
Zn _{0.5} Cd _{0.5} S/MnO ₂ (20mg)	Water (20 mL)	16	24	46.6	46.6	6.2	14
Pt/g-C ₃ N ₄ (10 mg)	ACN (10mL)	10	48	38.4	38.4	0.8	15
CdS/Mn(NO ₃) ₂ (40 mg)	ACN (2 mL)	25	48	99	99	1.0	16
ZnIn ₂ S ₄ /Nb ₂ O ₅ (50 mg)	BTF (5 mL)	10	6	21.6	19.1	1.6	17
g-C ₃ N ₄ @WO ₃ -MnO ₂ (15 mg)	ACN (30 mL)	24	24	77.6	61.2	18.3	18
Ru complex/CdS (10 mg)	DMF (10 mL)	10	22	81	74.5	3.4	19
Bi ₂ WO ₆ (20 mg)	ACN (5 mL)	10	10	58.3	58	2.9	20
Bi ₂ WO ₆ (20 mg)	BTF (5 mL)	10	10	46.7	46.3	2.3	20
Cu ₁ /p-CNS (5 mg)	ACN (5 mL)	10	24	77.1	66	1.38	21
Nb ₂ O ₅ /g-C ₃ N ₄ (25 mg)	ACN (10 mL)	1	5	72.6	61	1.22	22
Cd _{0.7} Zn _{0.3} S/NiSe (10 mg)	ACN (3 mL)	30	11	-	-	17.3	23
Decatungstate (5mg)	ACN (5.5 mL)	0.5	12	87.7	67.1	3.69	24
Cs ₂ SnBr ₆ /rGO (15 mg)	ACN (10 mL)	5	12	99.5	88	3.67	25
ZnIn ₂ S ₄ (10 mg)	ACN (2 mL)	10	2	95.7	69.4	6.94	26
Perylene imide/ZnIn ₂ S ₄ (20 mg)	ACN (10 mL)	2	1	97.7	89.8	17.9	27
(110)/(102) ZnIn ₂ S ₄ (20 mg)	ACN (10 mL)	5	1	91.1	90.5	45.3	28
Co ₁ /ZnIn ₂ S ₄ (15 mg)	ACN (15 mL)	5	12	98.6	91.1	5.25	29
Cd _{0.75} Zn _{0.25} S (20 mg)	ACN/H ₂ O (10 mL)	50	12	>90	65	27.5	This work

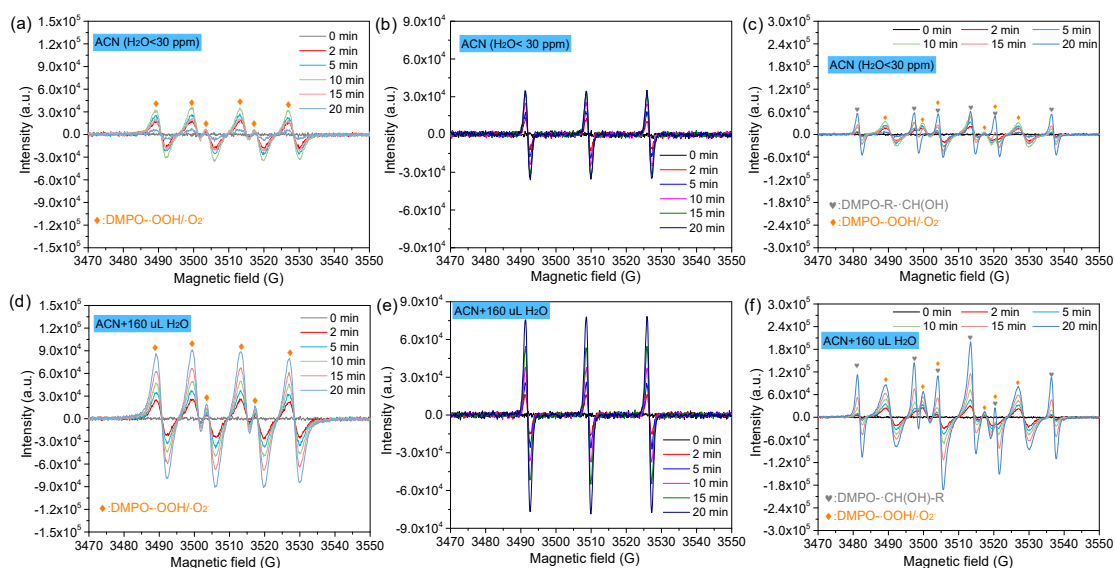


Fig.S13 In situ electron spin resonance trapping of $\cdot\text{O}_2/\cdot\text{OOH}$, $^1\text{O}_2$, and $\text{R}\cdot\text{-CHOH}$ in ACN (a-c) and ACN + 160 μL H_2O (d-f) over bare $\text{Cd}_{0.75}\text{Zn}_{0.25}\text{S}$.

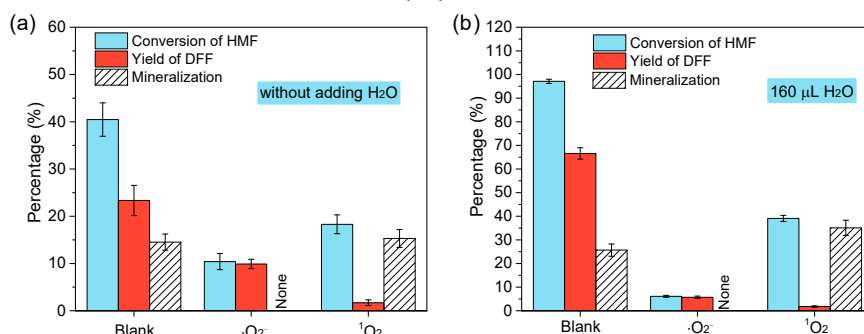


Fig.S14 Trapping experiments of $\cdot\text{O}_2$ and $^1\text{O}_2$ in ACN and ACN + 160 μL H_2O over bare $\text{Cd}_{0.75}\text{Zn}_{0.25}\text{S}$.

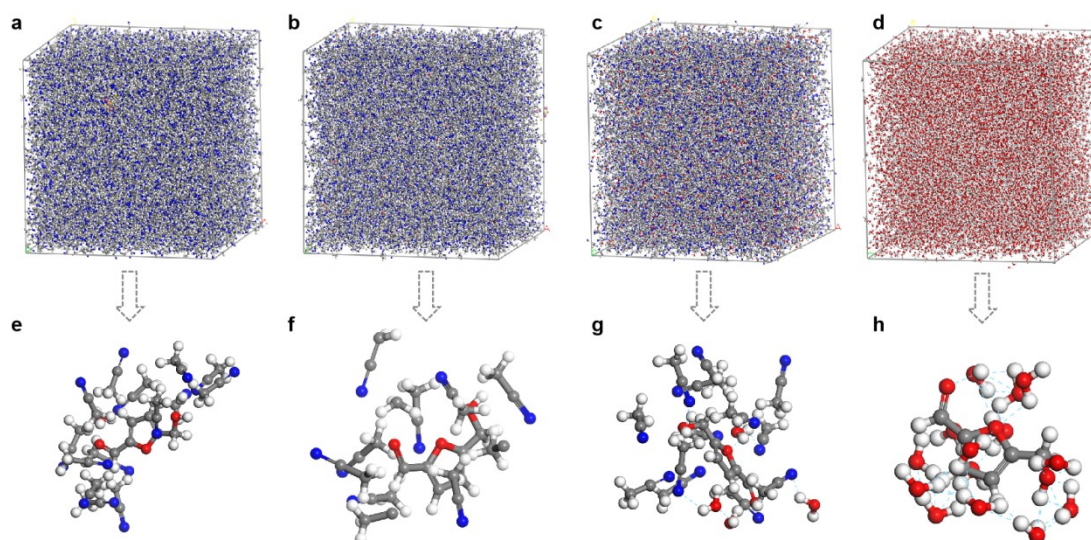


Fig.S15 Molecular dynamics (MD) simulation of the solvent: Solvation models of different solvents containing HMF: (a) Pure ACN, (b) ACN+160 μL H_2O , (c) ACN+1.7 mL H_2O . (d) pure H_2O . (e-f) Localized Solvation structure of HMF in different solvent systems: (e) Pure ACN, (f) ACN+160 μL H_2O , (g) ACN+1.7 mL H_2O . (h) pure H_2 (blue ball: N, white ball: H, gray ball: C, red ball: O, blue dash: H-bonding)

Tab.S5 The average H-bonding number in different solvent composition.

Solvent	Average Number of H bonding	Bond length (nm)
Pure ACN	0	-
ACN+160 uL H ₂ O	0	0.774
ACN+1.7 mL H ₂ O	3.3	0.328
Pure H ₂ O	33.9	0.226

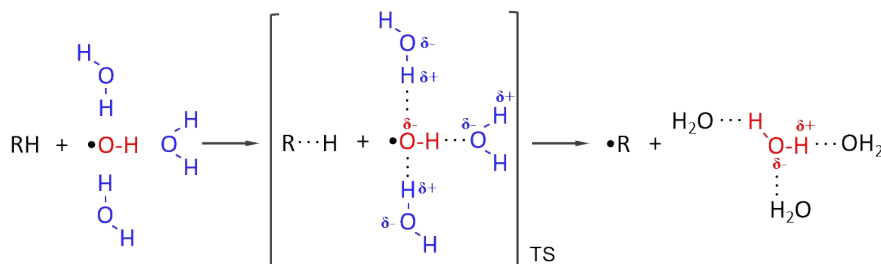


Fig.S16 Schematic diagram of the stabilization effect of water on the transition state of $\cdot\text{OH}$ ³³

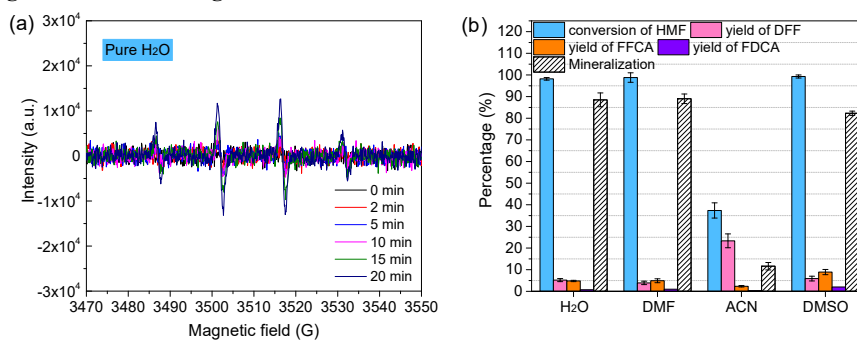


Fig.S17 (a) Electron spin resonance trapping in pure H₂O using bare Cd_{0.75}Zn_{0.25}S, (b) HMF oxidation performance of Cd_{0.75}Zn_{0.25}S in different solvent (HPLC grade ACN with 30 ppm water, DMF with H₂O content lower than 0.1 %, DMSO with H₂O content lower than 0.2 %).

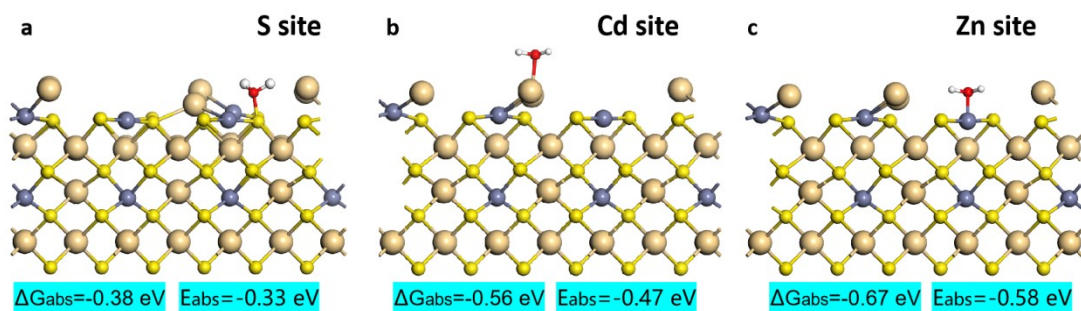


Fig.S18 Absorption structure of H₂O on the different sites of Cd_{0.75}Zn_{0.25}S (002) (a: S site, b: Cd site, c: Zn site), The results show that H₂O exhibits a most favorable absorption site on Zn atom.

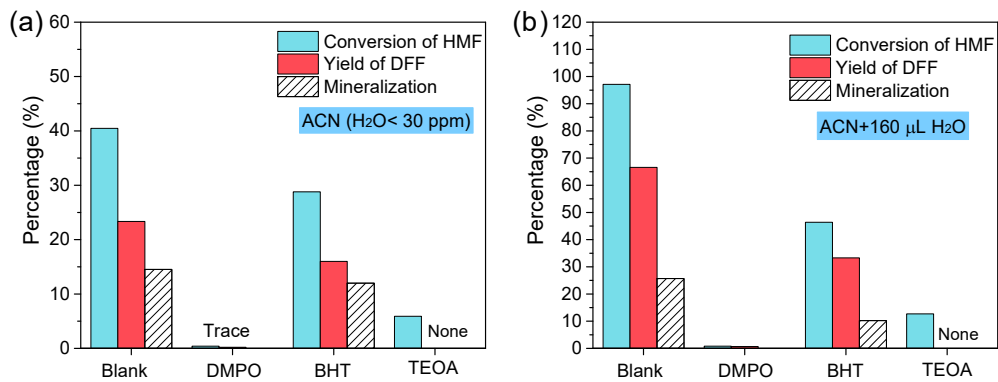


Fig.S19 (a-b) HMF conversion, DFF yield and mineralization on bare Cd_{0.75}Zn_{0.25}S after trapping in the presence of radicals' scavenger DMPO and R·CH(OH) scavenger BHT, hole scavenger TEOA in ACN and ACN + 160 μL H₂O.

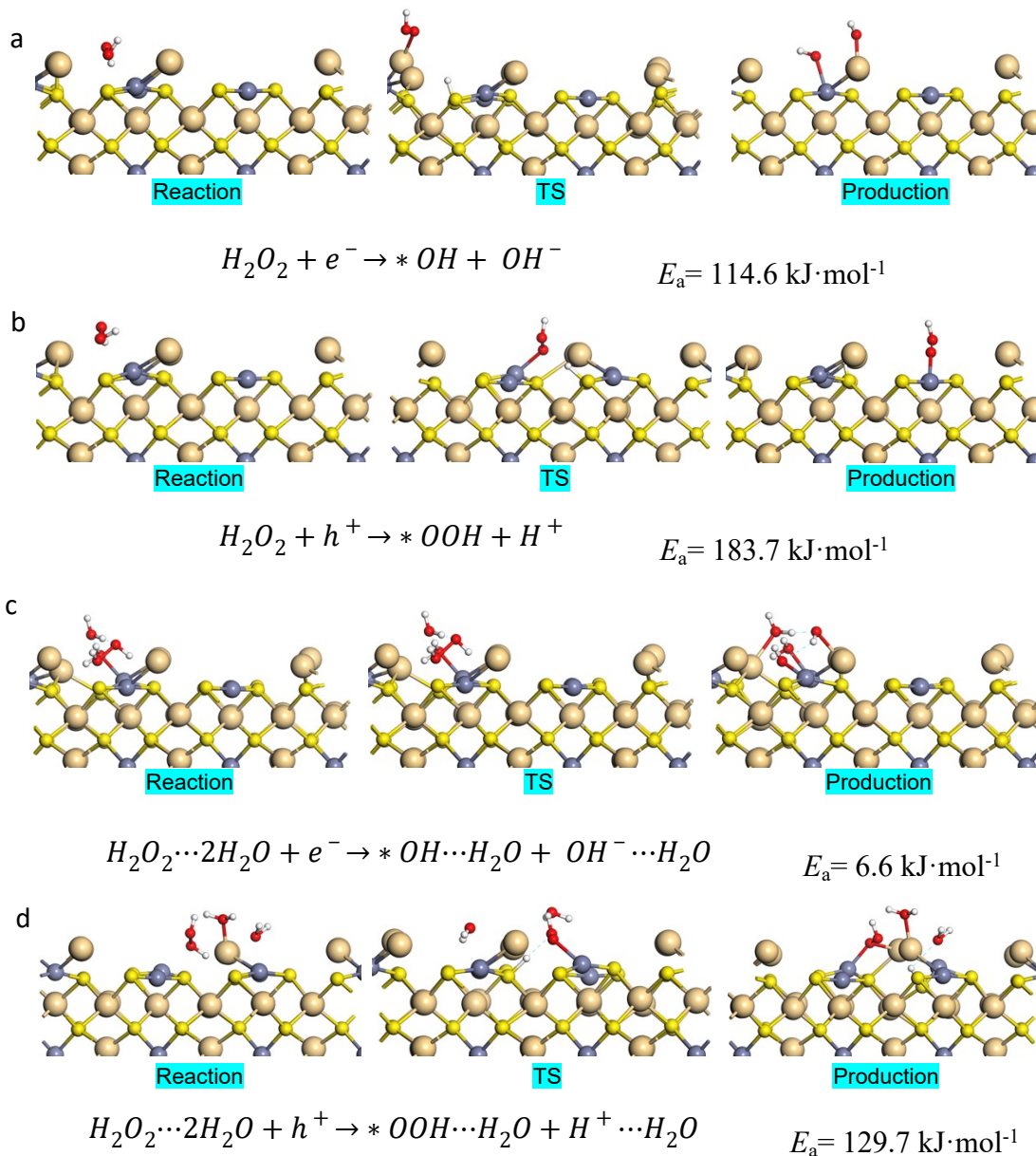


Fig.S20 DFT result of H_2O_2 decomposition energy barriers on the surface of CZS (002) with(a-b) or without (c-d) water involving (yellow: S, pale yellow: Cd, dark blue: Zn).

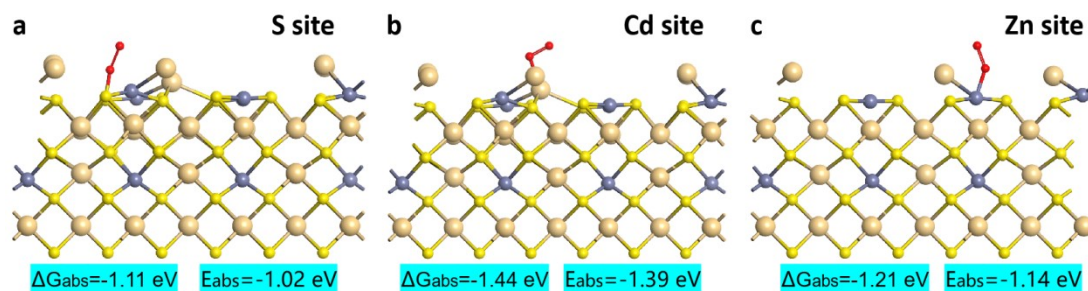


Fig.S21 Absorption structure of O_2 on the different sites of $\text{Cd}_{0.75}\text{Zn}_{0.25}\text{S}$ (002) (a: S site, b: Cd site, c: Zn site).

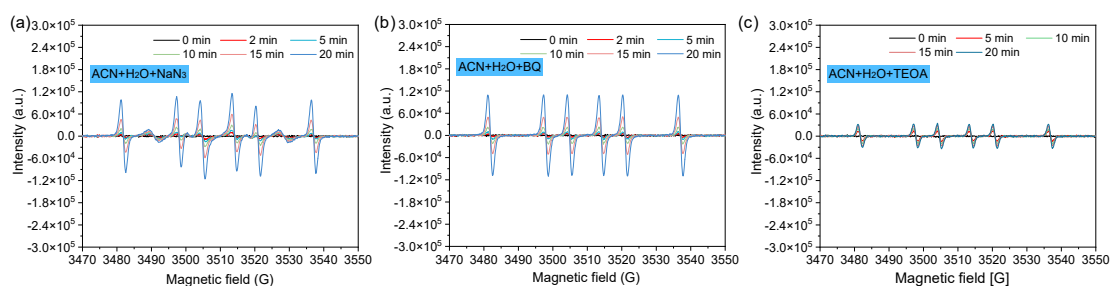


Fig.S22 (a) Electron spin resonance trapping of $\text{R}\cdot\text{CHOH}$ ACN + 160 μL H_2O in the presence of $\cdot\text{O}_2$, $^1\text{O}_2$ and holes scavengers using bare $\text{Cd}_{0.75}\text{Zn}_{0.25}\text{S}$.

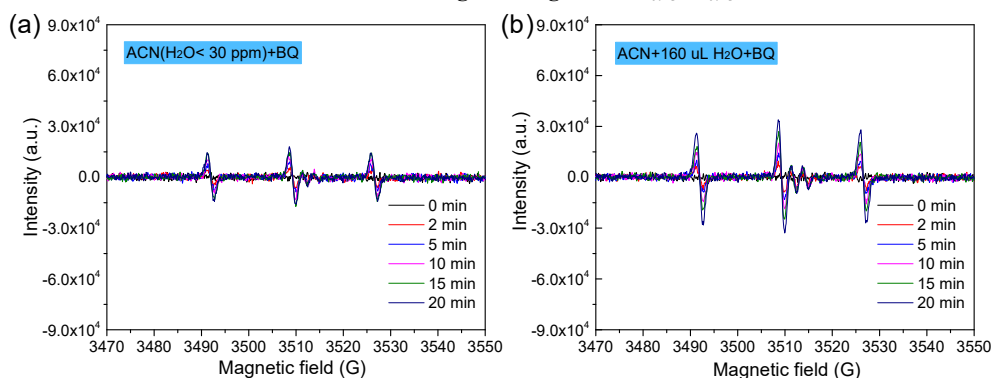


Fig.S23 (a) Electron spin resonance trapping of $^1\text{O}_2$ in ACN and ACN + 160 μL H_2O using bare $\text{Cd}_{0.75}\text{Zn}_{0.25}\text{S}$.

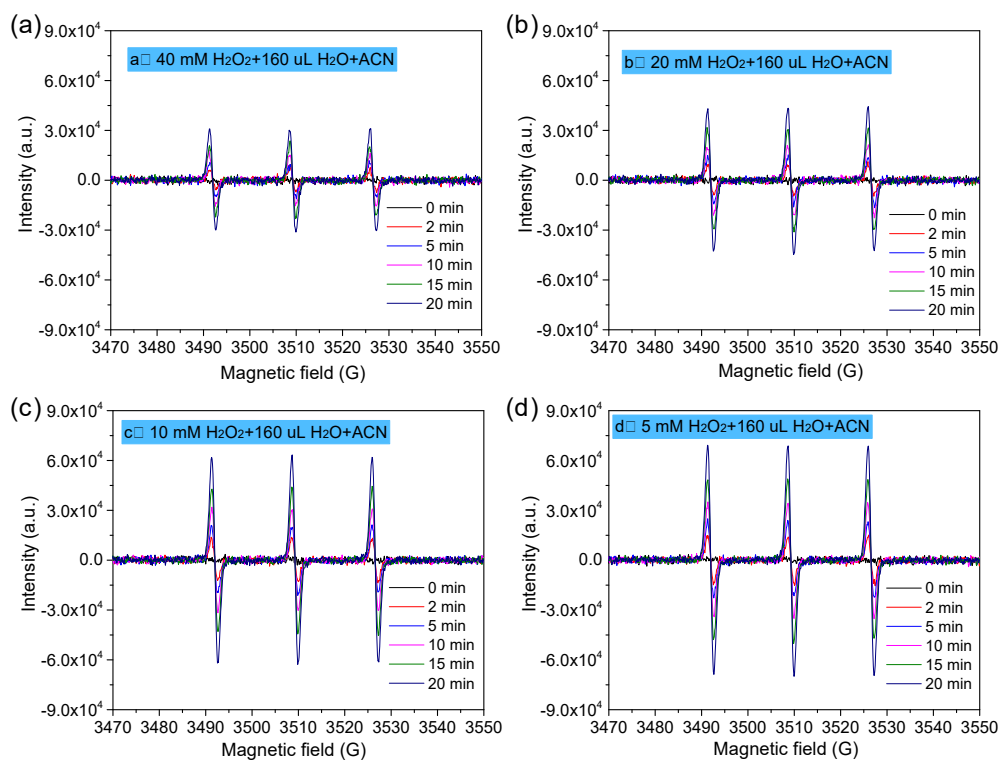


Fig.S24 Electron spin resonance trapping of $^1\text{O}_2$ in ACN + 160 μL H_2O in the presence different amount H_2O_2 using bare $\text{Cd}_{0.75}\text{Zn}_{0.25}\text{S}$.

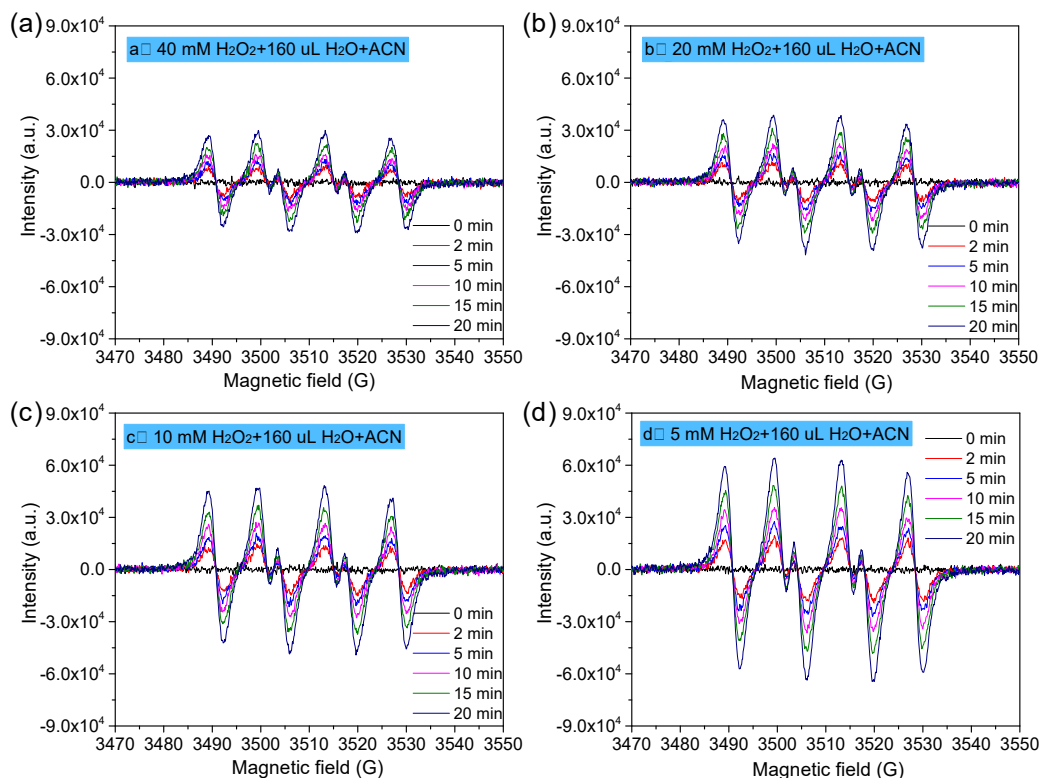


Fig.S25 Electron spin resonance trapping of $\cdot\text{O}_2^-$ in ACN + 160 μL H_2O in the presence different amount H_2O_2 using bare $\text{Cd}_{0.75}\text{Zn}_{0.25}\text{S}$.

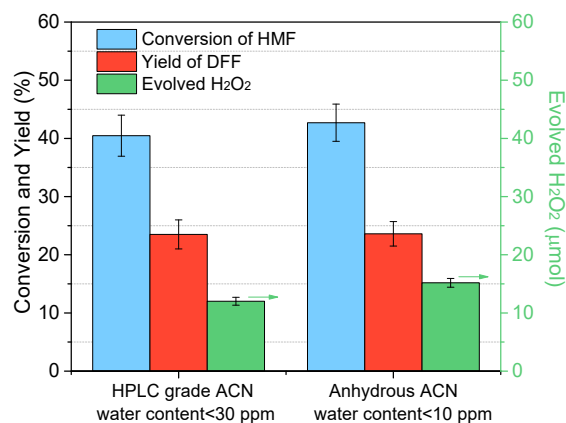


Fig.S26 Comparison of HMF conversion on bare Cd_{0.75}Zn_{0.25}S, DFF yield and H₂O₂ productivity in different ACN: (a) HPLC grade (water content < 30 ppm); (b) Anhydrous ACN (water content < 10 ppm).

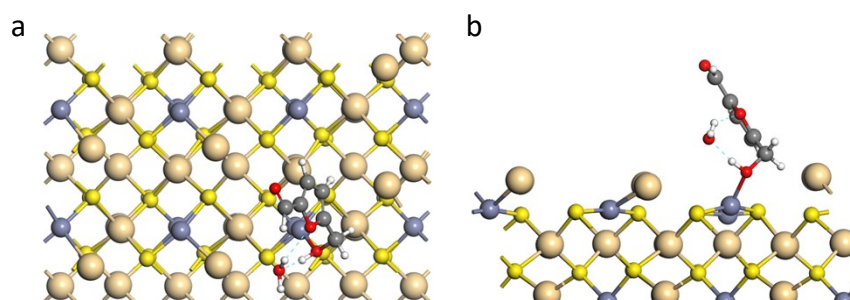


Fig.S27 Optimized absorption structure of HMF in the presence of water with H-bonding interaction (a:top view, b: side view, yellow: S, pale yellow: Cd, dark blue: Zn)

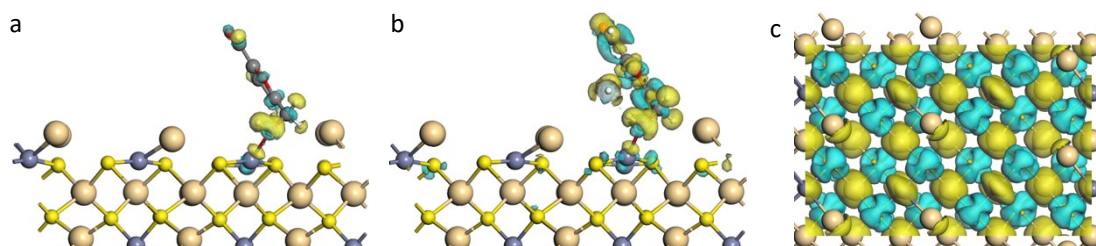
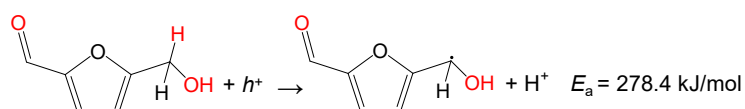
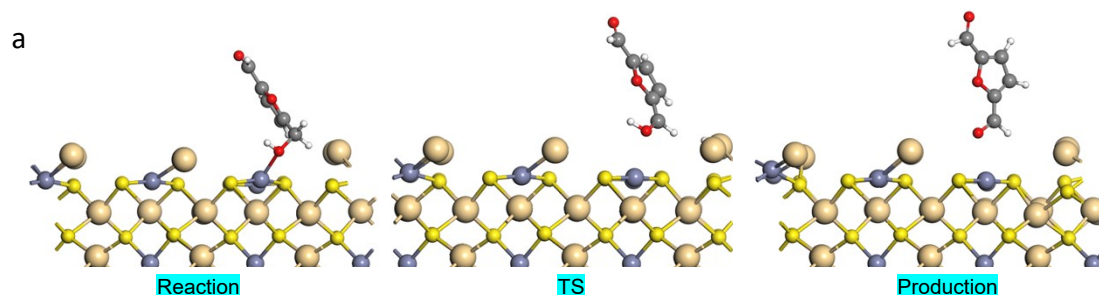


Fig.S28 Charge distribution analysis near surface of Cd_{0.75}Zn_{0.25}S(002) for HMF absorption in the (a) absence and/or (b) presence of H-bonding, (c) Difference charge density of bare Cd_{0.75}Zn_{0.25}S(002, top view), blue region is electron accumulation, Yellow is electron loss region (yellow: S, pale yellow: Cd, dark blue: Zn)



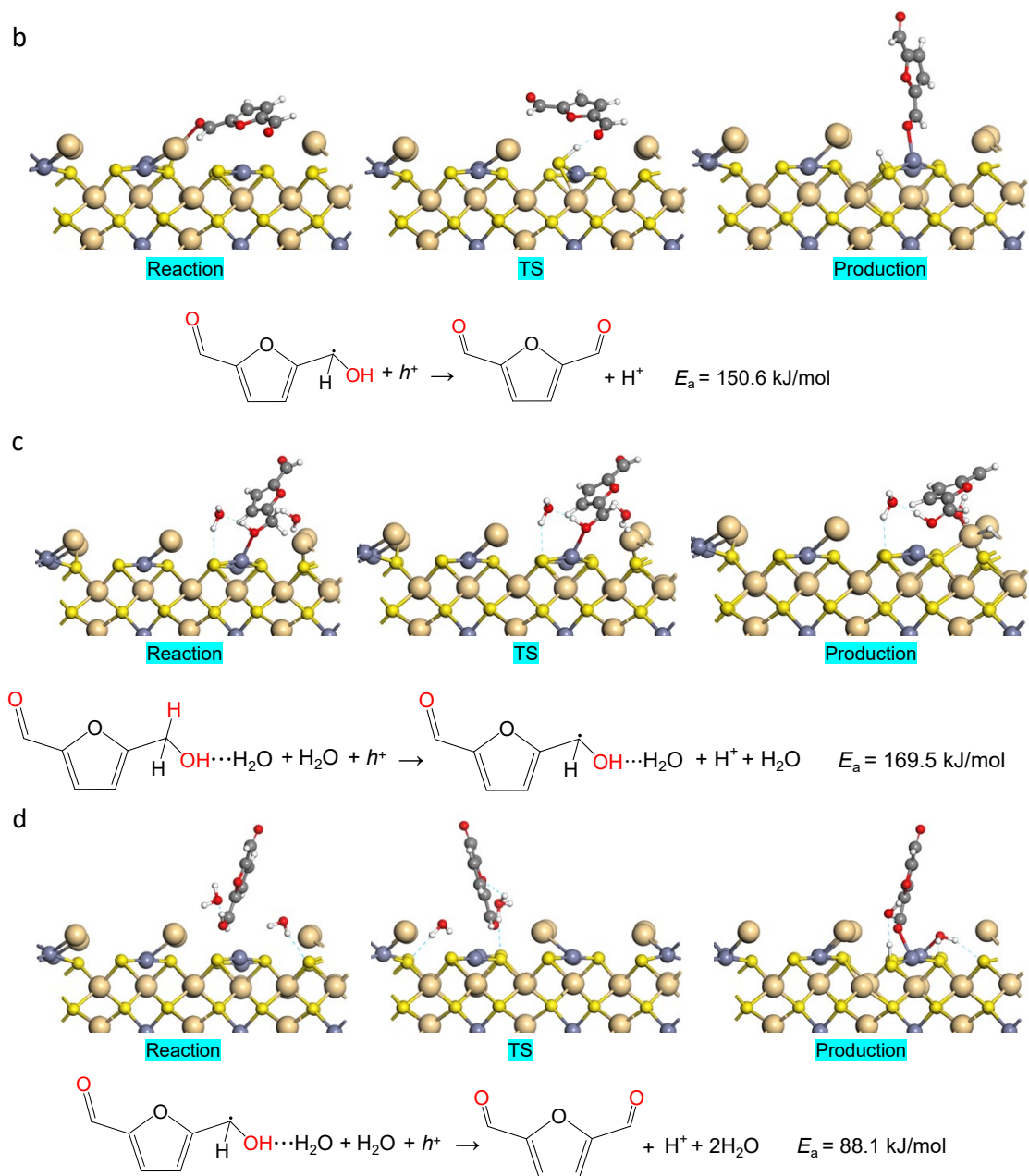


Fig. S29 The activation of C-H and O-H bond in HMF in the absence (a-b) and presence (c-d) of surface water via H-bonding (the blue dash line is H-bonding, yellow: S, pale yellow: Cd, dark blue: Zn)

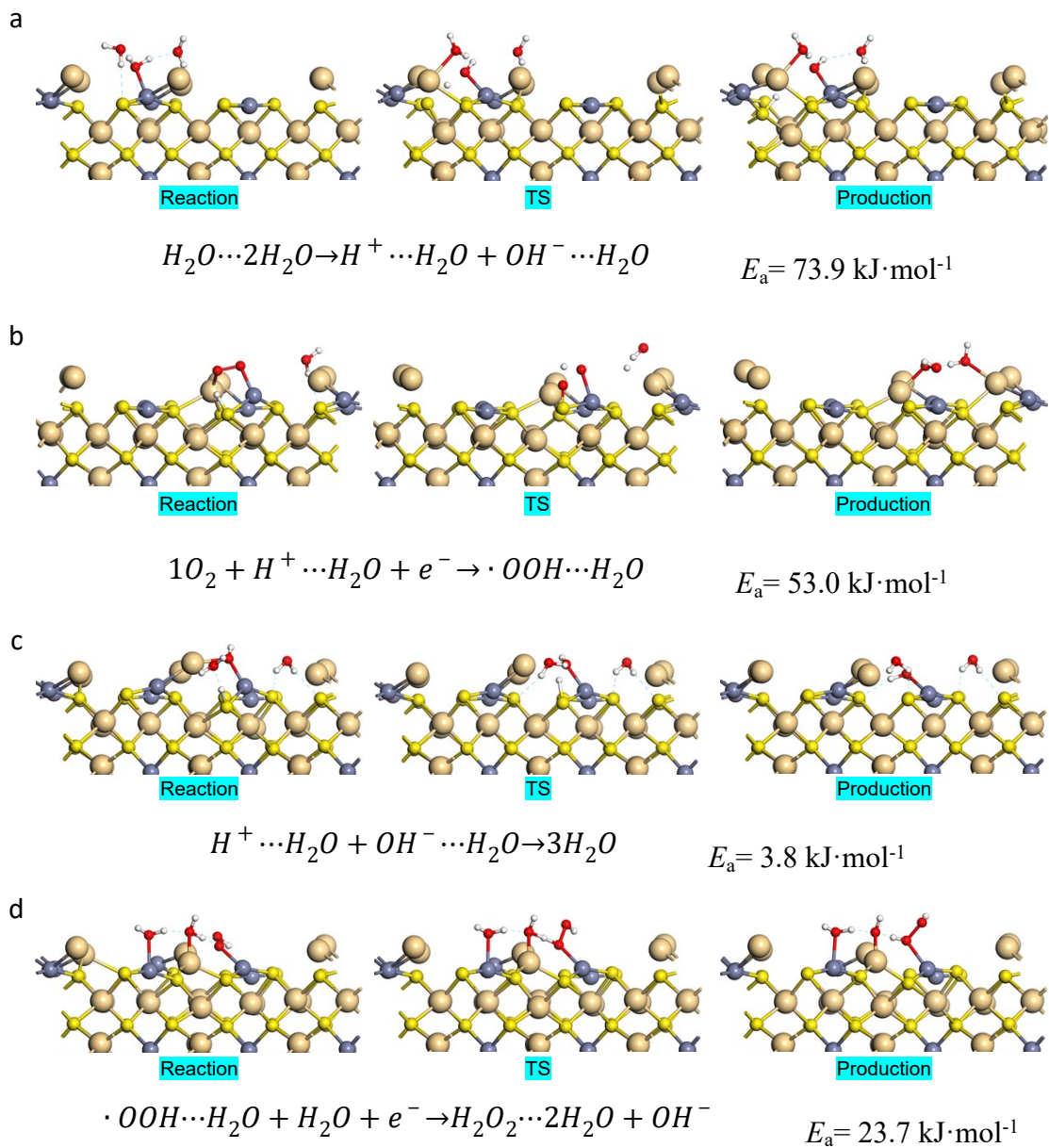


Fig. S30 The activation of (a)water dissociation, (b) $\cdot OOH$ generation, (c)water regeneration, and (d) H_2O_2 generation in the presence surface water.

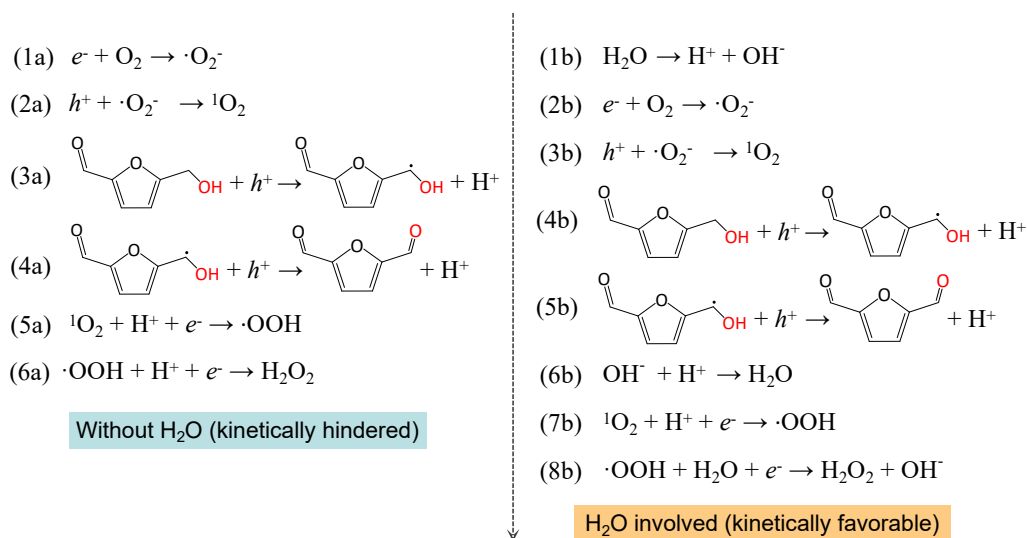


Fig.S31 The reaction pathways of HMF to DFF in the presence and absence of water.

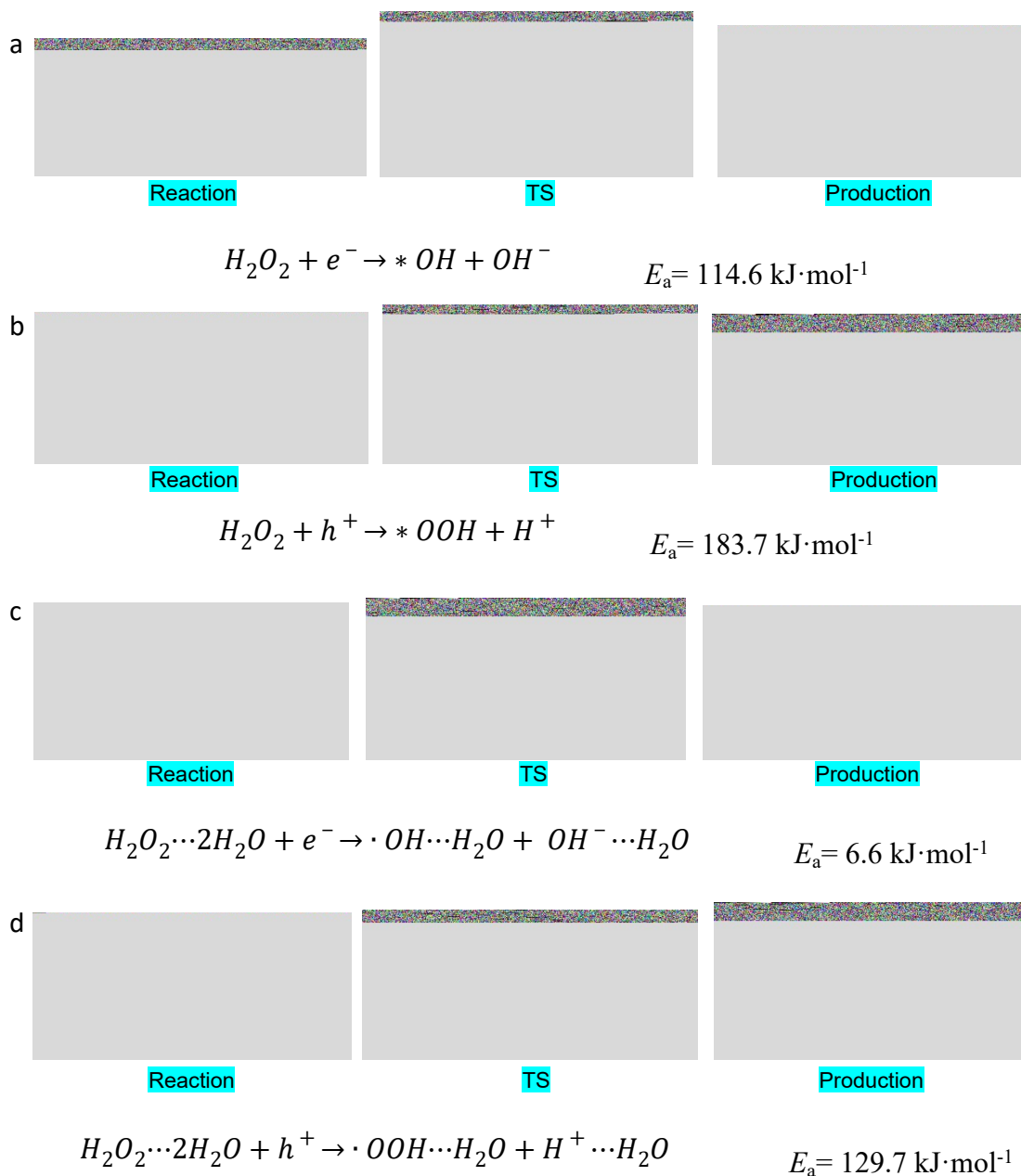


Fig S32 The H₂O₂ decomposition energy barriers in the absence (a, b) and presence (c, d) of surface water.

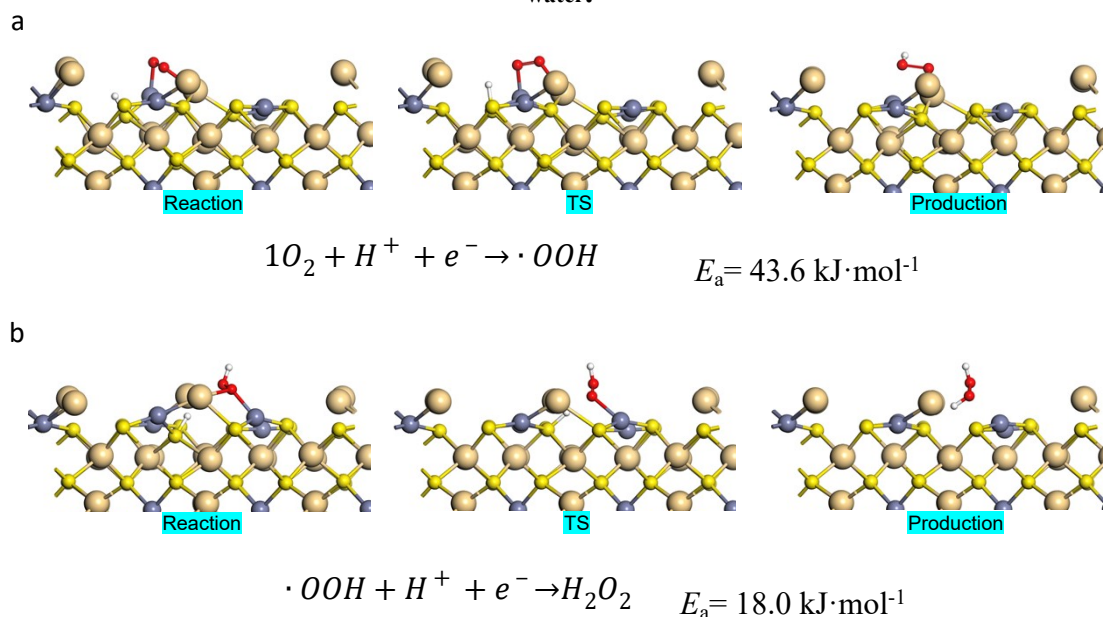
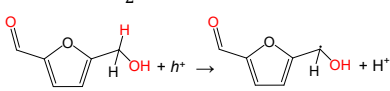
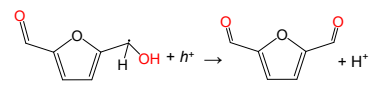


Fig. S33 The activation energy of (a) ·OOH generation and (b) H₂O₂ generation in the absence surface hydrogen bonding interaction.

Tab. S6 The activation barriers (kJ/mol) for the oxidation of HMF with or without H₂O.

	Reactions	E _a (kJ/mol)	
		Without H ₂ O	H ₂ O involved
1b	$2H_2O \rightarrow H^+ + OH^-$	-	73.9
2		278.4	169.5
3		150.6	88.1
4	$1O_2 + H^+ + e^- \rightarrow \cdot OO H$	42.6	53.0
5	$\cdot OO H + H^+ + e^- \rightarrow H_2O_2$	18.0	-
5b	$\cdot OO H + H_2O + e^- \rightarrow H_2O_2 + OH^-$	-	23.7
6	$H_2O_2 + e^- \rightarrow \cdot OH + OH^-$	114.6	6.6
7	$H_2O_2 + h^+ \rightarrow \cdot OO H + H^+$	183.7	129.7
8b	$H^+ + OH^- \rightarrow H_2O$	-	3.8

b: The elementary step occurs only in the presence of water

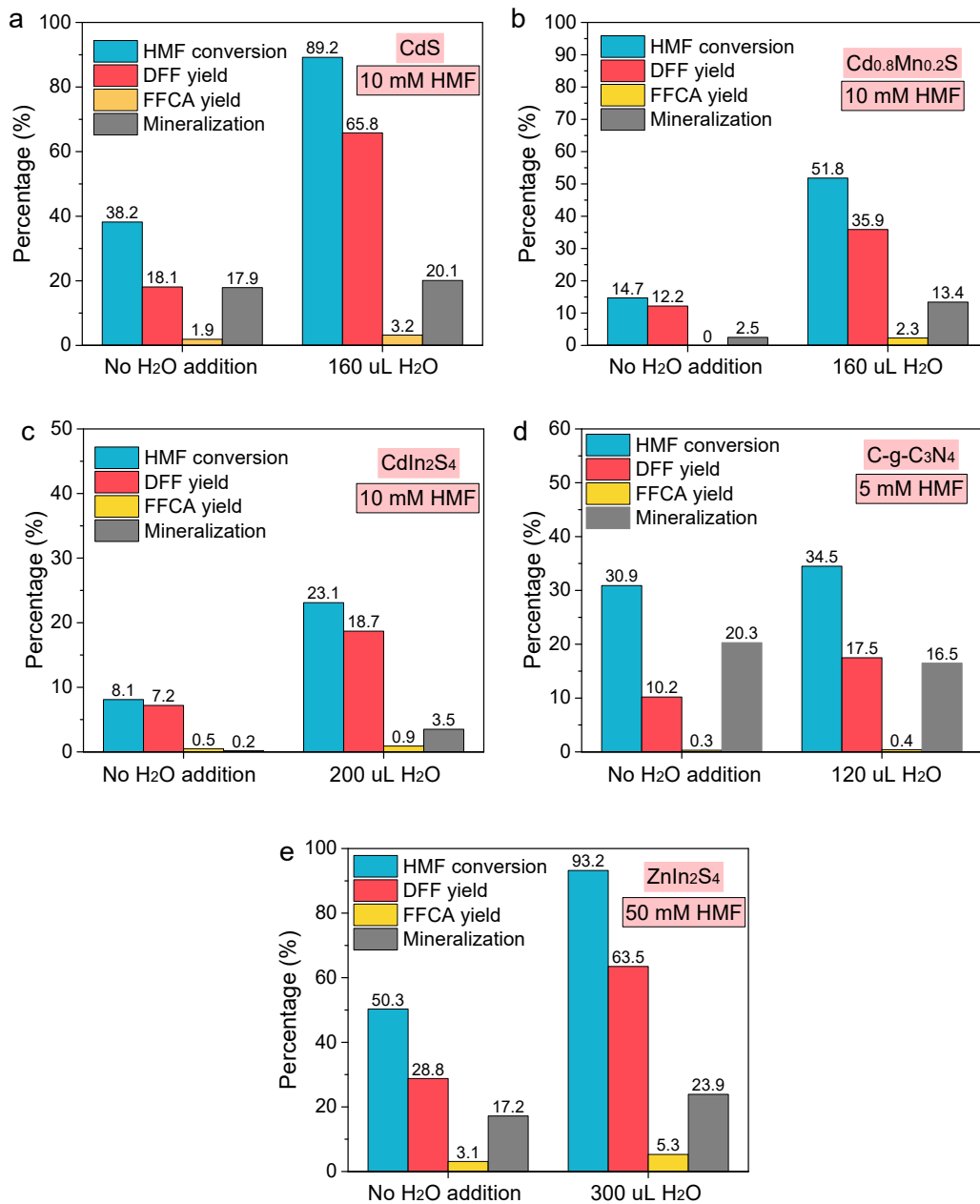


Fig. S34 The applicability of the water-addition strategy to other photocatalysts.

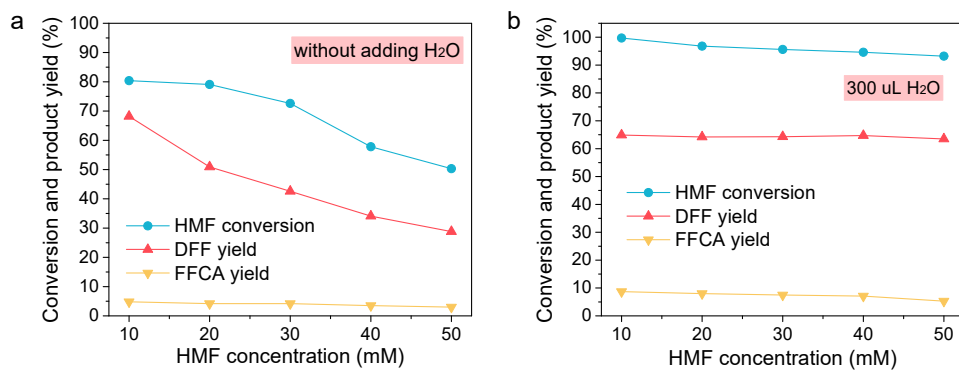
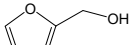
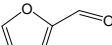
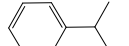
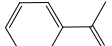
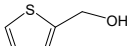
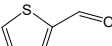
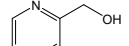
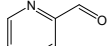
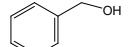
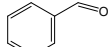
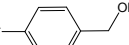
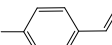
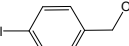
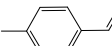
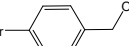
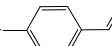
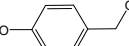





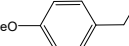
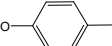
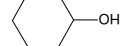
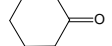
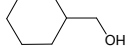
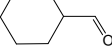


Fig. S35 The conversion and products yield of ZnIn₂S₄ with different HMF concentration (a: without adding water, b: 300 uL water)

Tab. S7 The conversion and product yield of different alcohol substrates with or without adding water in ACN

Substrates	Products	ACN		ACN+160 uL H ₂ O	
		Con. (%)	Yield (%)	Con. (%)	Yield (%)
		54.3	17.9	98.5	48.0
		26.6	26.2	58.5	53.4
		80.2	50.6	>99	67.6
		85.0	56.7	>99	76.6
		51.5	48.7	97.0	80.6
		61.2	60.4	97.8	89.6
		62.9	58.1	>99	88.4
		66.2	58.0	>99	75.9
		60.5	30.1	>99	63.5
		39.7	32.5	>99	84.2
		65.7	48.6	>99	69.0
		74.4	37.8	>99	52.1
		4.8	1.9	15	8.8
		3.2	1.0	12.4	6.5

References

- H. Wang, M. Bootharaju, J. Kim, Y. Wang, K. Wang, M. Zhao, R. Zhang, J. Xu, T. Hyeon, X. Wang, *J. Am. Chem. Soc.*, 2023, **145**, 2264-2270.
- F. Fan, Z. Chen, A. Zhou, Z. Yang, Y. Zhang, X. He, J. Kang, W. Zhou, *Fuel*, 2023, **333**, 126351.
- J. Vincent, P. Crozier, *Nat. Commun.*, 2021, **12**, 5789.
- J. Wang, D. Cheng, F. Chen, X. Zhan, *ACS. Catal*, 2022, **12**, 4501-4516.
- M. Bikerouin, O. Chdil, M. Balli, *Nanoscale*, 2015, **15**, 7126-7138.
- Y. Xie, J. Wu, G. Jing, H. Zhang, S. Zeng, X. Tian, X. Zou, J. Wen, H. Su, C. Zhong, P. Cui, *Appl. Catal. B*, 2018, **239**, 665-676.
- Y. Pan, Y. Chen, K. Wu, Z. Chen, S. Liu, X. Cao, W. Cheong, T. Meng, J. Luo, L. Zheng, C. Liu, D. Wang, Q. Peng, J. Li, C. Chen, *Nat. Commun.*, 2019, **10**, 4290.
- G. Han, F. Li, A. Rykov, Y. Im, S. Yu, J. Jeon, S. Kim, W. Zhou, R. Ge, Z. Ao, T. Shin, J. Wang, H. Y. Jeong, J. Baek, *Nat. Nanotechnol.*, 2022, **17**, 403-407.
- M. Zhang, Z. Li, X. Xin, J. Zhang, Y. Feng, H. Lv, *ACS Catal.*, 2020, **10**, 14793-

14800.

10. H. Zhang, Q. Wu, C. Guo, Y. Wu, T. Wu, *ACS Sustainable Chem. Eng.* 2017, **5**, 3517-3523.
11. H. Zhang, Z. Feng, Y. Zhu, Y. Wu, T. Wu, *J. Photochem. Photobiol., A*, 2019, **371**, 1-9.
12. H. Ye, R. Shi, X. Yang, W. Fu, Y. Chen, *Appl. Catal., B*, 2018, **233**, 70-79.
13. S. Yurdakal, B. Tek, O. Alagöz, V. Augugliaro, V. Loddo, G. Palmisano, L. Palmisano, *ACS Sustainable Chem. Eng.* 2013, **1**, 456-461.
14. S. Dhingra, T. Chhabra, V. Krishnan, C. Nagaraja, *ACS Appl. Energy Mater.*, 2020, **3**, 7138-7148.
15. V. Battula, A. Jaryal, K. Kailasam, *J. Mater. Chem. A*, 2019, **7**, 5643-5649.
16. J. DiMeglio, A. Breuhaus-Alvarez, S. Li, B. Bartlett, *ACS Catal.*, 2019, **9**, 5732-5741.
17. Y. Wang, X. Kong, M. Jiang, F. Zhang, X. Lei, *Inorg Chem. Front.*, 2020, **7**, 437-446.
18. H. Qian, Q. Hou, W. Zhang, Y. Nie, R. Lai, H. Ren, G. Yu, X. Bai, H. Wang, M. Ju, *Appl. Catal. B: Environ*, 2022, **319**, 121907.
19. T. Xia, W. Gong, Y. Chen, M. Duan, J. Ma, X. Cui, Y. Dai, C. Gao, Y. Xiong, *Angew. Chem. Int. Ed.*, 2022, **61**, e202204225.
20. A. Kumar, R. Srivastava, *ACS Appl. Nano Mater.*, 2021, **4**, 9080-9093.
21. G. Wang, R. Huang, J. Zhang, J. Mao, D. Wang, Y. Li, *Adv. Mater.* 2021, **33**, 2105904.
22. S. Sharma, S. Kumar, S. Arumugam, M. Palanisami, V. Shanmugam, S. Elumalai, *ChemPhotoChem*, 2021, **5**, 1-11.
23. T. Shan, L. Luo, T.n Chen, L. Deng, M. Li, X. Yang, L. Shen, M. Yang, *Green Chem.*, 2023, **25**, 2745-2756.
24. B. Yang, W. Hu, F. Wan, C. Zhang, Z. Fu, A. Su, M. Chen, Y. Liu, *Chem. Eng. J.*, 2020, **396**, 125345.
25. L. Yin, Y. Wu, X. Bao, X. Liu, D. Dai, M. Zhang, Z. Wang, Z. Zheng, Y. Liu, H. Cheng, Y. Dai, B. Huang, P. Wang, *Chem. Eur. J.* 2023, **29**, e202300999.
26. S. Ding, J. Filho, T. Peppel, S. Haida, J. Rabeah, N. Steinfeldt, J. Strunk, *Sustain. Energ. Fuels*, 2023, **7**, 4396.
27. Y. Guo, B. Liu, J. Zhang, G. Wang, C. Pan, H. Zhao, C. Wang, F. Yu, Y. Dong, Y. Zhu, *Appl. Catal. B: Environ.*, 2024, **340**, 123217.
28. H. Zhao, D. Trivedi, M. Roostaenia, X. Yong, J. Chen, P. Kumar, J. Liu, B. Su, S. Larter, M. Kibria, J. Hu, *Green Chem.*, 2023, **25**, 692.
29. X. Tan, S. Si, D. Xiao, X. Bao, K. Song, Z. Wang, Y. Liu, Z. Zheng, P. Wang, Y. Dai, B. Huang, H. Cheng, *ACS Catal.* 2023, **13**, 14395-14403.
30. L. Ma, M. Liu, D. Jing, L. Guo, *J. Mater. Chem. A*, 2015, **3**, 5701-5707.
31. L. Ma, T. Zhang, R. Song, L. Guo, *Int. J. Hydrogen. Energ.* 2018, **431**, 3778-3787.
32. D. Wakerley, M. Kuehnel, K. Orchard, K. Ly, T. Rosser, E. Reisner, *Nat. Energy*, 2017, **2**, 17021.
33. S. Mitroka, S. Zimmeck, D. Troya, J. Tanko, *J. Am. Chem. Soc.*, 2010, **132**, 2907-2913.